Hindawi Publishing Corporation
International Journal of Antennas and Propagation
Volume 2015, Article ID 830920, 10 pages
http://dx.doi.org/10.1155/2015/830920

Research Article

A Compact Two-Level Sequentially Rotated Circularly Polarized Antenna Array for *C*-Band Applications

Stefano Maddio

Department of Information Engineering, University of Florence, V.S. Marta 3, 50139 Florence, Italy

Correspondence should be addressed to Stefano Maddio; stefano.maddio@unifi.it

Received 27 July 2015; Revised 25 October 2015; Accepted 28 October 2015

Academic Editor: Ikmo Park

A compact circular polarized antenna array with a convenient gain/bandwidth/dimension trade-off is proposed for applications in the *C*-band. The design is based on the recursive application of the sequential phase architecture, resulting in a 4×4 array of closely packed identical antennas. The 16 antenna elements are disc-based patches operating in modal degeneration, tuned to exhibit a broad while imperfect polarization. Exploiting the compact dimension of the patches and a space-filling design for the feeding network, the entire array is designed to minimize the occupied area. A prototype of the proposed array is fabricated with standard photoetching procedure in a single-layer via less printed board of overall area $80 \times 80\,\text{mm}^2$. Adequate left-hand polarization is observed over a wide bandwidth, demonstrating a convenient trade-off between bandwidth and axial ratio. Satisfying experimental results validate the proposed design, with a peak gain of 12.6 dB at 6.7 GHz maintained within 3 dB for 1 GHz, a very wide 10 dB return loss bandwidth of 3 GHz, and a 4 dB axial ratio bandwidth of 1.82 GHz, meaning 31% of fractional bandwidth.

1. Introduction

Modern wireless and mobile communication systems as well as remote sensing applications have pushed the limits of printed antenna technology. While widely employed for their inherent advantages in terms of low profile, conformability, light weight, and low manufacturing cost, the narrow bandwidth limit of printed antennas is still of concern. Over the last decade, there have been considerable efforts toward finding solutions for this issue. A good example is the use of nonresonant structures like vivaldi antennas [1] or wideband monopole [2].

Antennas operating in circular polarization (CP) offer even more interesting features, like robustness against adverse weather conditions and the capability to communicate regardless of source and target relative orientation. These characteristics make CP antennas the best candidates for outdoor communication systems [3–5], as well as emerging and nonconventional indoor applications [6, 7]. Furthermore, a wide range of applications in the *C*-band, such as Dedicated Short Range Communication for Electronic Toll Collection and the emerging Intelligent Transportation System, are in need of cost-effective and lightweight CP antennas. Compactness, wide band, and robustness are stricter needs than high gain and extreme polarization purity, [8].

Unfortunately, printed CP antennas suffer even more critical bandwidth limits in comparison to linearly polarized (LP) antennas. The bandwidth issue is of particular concern in antennas designed exploiting the mechanism of modal degeneration [9], which is popular for the compact dimension. Sequential Phase Architecture (SPA) is a well-known approach to improve CP bandwidth. It consists in the rotation of antenna elements fed with a 90° progressive phase [10, 11]. The SPA technique can be applied to a broad range of elementary antennas, such as printed dipoles [11], vivaldi antennas [12], slot antennas [13], patch antennas [10], and many more [14, 15]. One of the most interesting features of the SPA approach is the fact that it can be reiterated, with subsequent enhancement of the polarization purity and gain [10, 16, 17].

In this paper a compact sequential antenna array operating in the *C*-band is proposed, analyzed, and fabricated. The array is composed of 16 elements arranged as a sequential array of 4 subarrays, which are designed as 2×2

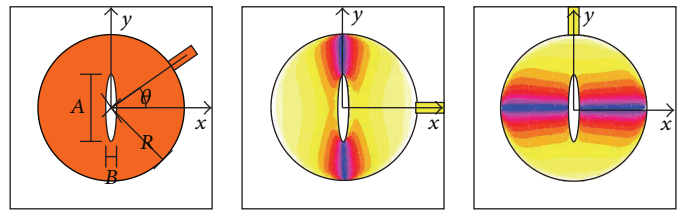

(a) Disc geometry (b) Mode TM_x (c) Mode TM_y

Figure 1: Patch characteristics and pictorial representation of the degenerated modes.

sequential phase arrays in turn. The basic element of the array is a compact disc-based patch antenna operating in modal degeneration. The feeding network is a space-filling Sequential Phase Network (SPN) structured in two levels. The elements are designed to exhibit a wide operation bandwidth, despite a suboptimal polarization performance and an input impedance characterized by a high variability. The use of SPN based on tapered lines grants the adequate power distribution, restoring appropriate gain and polarization performance over a wide bandwidth.

A single-layer via-less prototype is printed on a board of overall volume of 80 mm × 80 mm × 1.6 mm. The prototype has been fabricated with standard photo-etching technique using high quality dielectric substrate (isola 408). Adequate matching between simulation and measurement is observed. A peak gain of 12.6 dB at the center frequency of 6.7 GHz is measured and maintained within 3 dB for 1 GHz, and a very wide 10 dB return loss bandwidth of 3 GHz, covering almost half of the *C*-band, is measured. A broad axial ratio below 4 dB, adequate for many applications in the *C*-band, is observed for more than 1.8 GHz.

This paper is organized in the following manner. The design of the antenna element is analyzed in Section 2; then SPN is described in Section 3. In Section 4 the array arrangement is presented. Then, in Section 5, the simulation and experimental verifications are shown, compared, and discussed. In Section 6, some final conclusions are drawn.

2. Element Design

The basic element of the array is a disc-based patch already presented by the authors [18, 19]. It consists in a disc-based patch centrally cut with a thin elliptical shaped slit, as depicted in Figure 1(a). The disc radius is indicated with R, the ellipse axes are labeled by A and B, and θ is the angle individuated by the feeding line with the direction of the ellipse major axis. The patch operates in modal degeneration with the central elliptical cut detuning the fundamental TM_{11} mode of the disc into two overlapping ones, labeled TM_x and TM_y, forced by the different current paths through the ellipse axes.

Different from the classic truncated corner square [9], which is typically used for SPA array based on printed patch antenna [10, 20], the proposed disc element exhibits more degrees of freedom, permitting a better trade-off between polarization purity and broadband operation. Fixing the radius R, the axes A and B quantitatively control the modal splitting, while θ modulates the response dictating the actual combination of the modes. This mechanism is well illustrated by the circuital equivalence approach. In the range of frequency around the fundamental resonance of the unperturbed disc, the input impedance can be seen as the sum of the two second-order resonators, which are the equivalent circuits of the two modes:

$$\begin{aligned} Z_{\text{in}} &= Z_x + Z_y \\ &= \frac{R_x(\theta)}{1 + jQ_x\left(f/f_x - f_x/f\right)} \\ &\quad + \frac{R_y(\theta)}{1 + jQ_y\left(f/f_y - f_y/f\right)}. \end{aligned} \tag{1}$$

The equivalent circuital parameters f_x, f_y, R_x, R_y, and Q_x, Q_y depend on the patch geometry, feed position, and substrate characteristics [9, 18, 19]. In particular, in [21], it was shown that f_x and f_y are inversely proportional to both R and $A \times B$, according to an almost polynomial law [21, eq 2], making the modal synthesis relatively easy.

The Z_x term is associated with the lower mode, labeled TM_x, and it is excited if $\theta = 0^\circ$, since $R_y(0^\circ) = 0$ (i.e., a zero of TM_y modal field is associated with this position) and $R_x(0^\circ) = R_x^{\max}$ (corresponding to the edge impedance of the patch). The modal eigenfunction depicted in Figure 1(b) presents a distribution similar to one of the unperturbed discs in the fundamental mode, and it is the source of linearly polarized x-directed far-field. In a similar manner, the term Z_y, associated with the upper mode TM_y which is orthogonal to the former, is excited if $\theta = 90^\circ$, being $R_y(90^\circ) = R_y^{\max}$ and $R_x(90^\circ) = 0$. Figure 1(c) shows the eigenfunction of TM_y, associated with a y-directed far-field. The two modes are excited according to the ratio of the modal response, which in turn depends on θ in the range $[0^\circ, 90^\circ]$.

Figure 2 depicts the characteristics of a disc element *critically tuned* to exhibit perfect modal recombination at the central frequency of 6.5 GHz. In particular Figure 2(a) depicts the disc input impedance. It can be observed that the modal responses are strongly overlapped: each peak is in the bandwidth of the other, separated by less than 500 MHz. At the intermediate frequency, corresponding roughly to 6.5 GHz, the two modes are excited with almost the same magnitude and phase quadrature, as it can be observed in

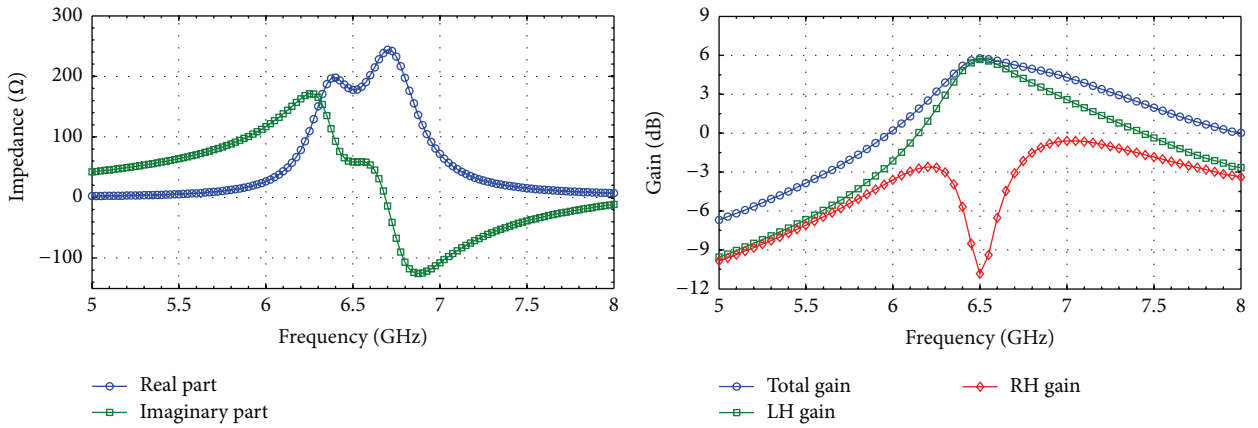

(a) De-embedded input impedance $Z_{in}(f) = Z_x(f) + Z_y(f)$. Continuous lines: real part, dotted lines: imaginary part

(b) Gain components. Total, left-hand, and right-hand

FIGURE 2: Critically tuned condition: the modal responses are perfectly combined about the center of their natural resonances.

Figure 2(b). Indeed, the total gain of the patch coincides with the left-hand CP component at the central frequency with about 6 dB, and the cross-polarized component is at least 17 dB below this level. This critical condition can occur only over a narrow band around the central frequency.

Recently, Zhang et al. [22] demonstrated that the use of elliptically polarized (EP) antennas can be successfully exploited in designing CP array based on SPA with better bandwidth performance than perfectly polarized antennas. The idea is to allow a broad though imperfect polarization, which can be enforced by a wideband SPN. In this way, nominal CP radiation can cover a wider bandwidth with respect to the case of critically polarized/narrowband antenna. In [22] it was demonstrated that the use of EP antennas with moderate axial ratio permits an increase of 3 dB axial ratio bandwidth up to 76%, when an ideal SPA network is employed.

Focusing on the proposed disc-patch design, a controlled detuning of the modes is more interesting than the critical condition, according to the previous reasoning. Figure 3(a) shows the input impedance of an *overtuned* disc. The two modal peaks are approximately 1 GHz apart in frequency; hence only partial modal superposition occurs. Indeed, the antenna is at the limit between imperfect CP operation and dual-band/dual-polarization operation. In this condition, the gain response in Figure 2(b) is obtained, with an almost constant, while imperfect, LH polarization over a wider band of frequency, much wider than the bandwidth of the critically tuned case in Figure 2.

The main drawback of this condition is the significant variability of the input impedance, which is difficult to match with canonic matching networks.

3. Sequential Phase Network Design

Figure 4(a) depicts the equivalent circuit of a canonic Sequential Phase Network (SPN), the feeding network enabling the SPA mechanism [10, 23]. In the case of 4 antennas, three cascading networks operate as Phase Shifter and Power Dividers (PSPDs), and four output matching networks (MNs) provide the adequate impedance transformation to match the four antennas to the outputs of the network.

With reference to Figure 4(a), at the first junction the available power P_0 from the source splits between the first output section and the rest of the network with a 1 : 4 ratio, that is, (1/4) P_0 in the first output and (3/4) P_0 in the remaining structure. At the second junction, the power ratio between the second output line and the rest of the network is 1 : 3, in order to have the same power toward the first and second antenna. At the next junction, the power splits in half, to excite the third and the fourth antennas.

In the canonic case, shown in Figure 4(b), the three PSPDs are implemented as transmission lines of 90°, which provide the required phase progression and also impedance transformation operating as quarter wave transformer (QWT). The output MNs are implemented as QWTs as well, exploiting the same matching property. Various implementations of this network can be found in the literature [16, 23].

To cope with the strongly resonant behavior of the antenna impedance, depicted in Figure 3(a), the solution introduced in [21, 24] and shown in Figure 4(c) is applied here. The main improvement regards the implementation of the four MNs as tapered lines instead of QWTs. While longer than 90°, tapered lines achieve enhanced impedance transformation which is more robust against impedance variation for a wider bandwidth.

To demonstrate the improvement, Figures 5 and 6 show the performance obtained with a canonic SPN based on QWTs in comparison to a tapered solution. For the sake of clarity the two designs are based on ideal transmission lines and tapers. The input impedance is 50 Ω, while the output impedance is 100 Ω; the latter is approximately the mean value of the resonances of the overtuned patch in Figure 3(a).

The canonic network is defined as follows (all in Ω): R_A = 138, R_B = 127, R_C = 96, R_D = 64, and $R_1 = R_2 = R_3$ = 55. The involved lines are 90° at center frequency, which is 6 GHz for the sake of clarity. The tapered solution is based on exponential tapers. Each taper starts with a different $R_{A,B,C,D}$

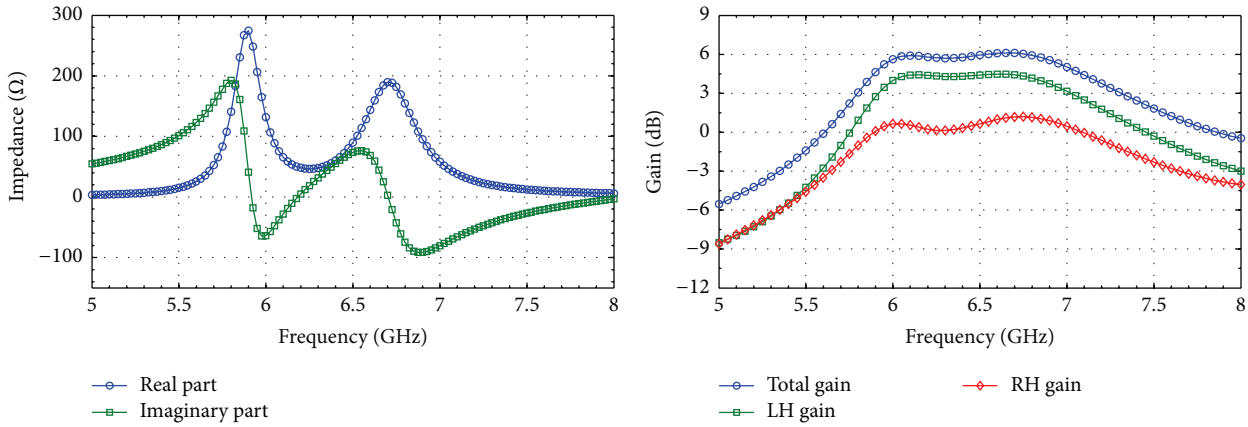

(a) De-embedded input impedance

(b) Gain components. Total, left-hand, and right-hand

FIGURE 3: Overtuned condition: the modal frequency is so apart that the perfect combination never occurs.

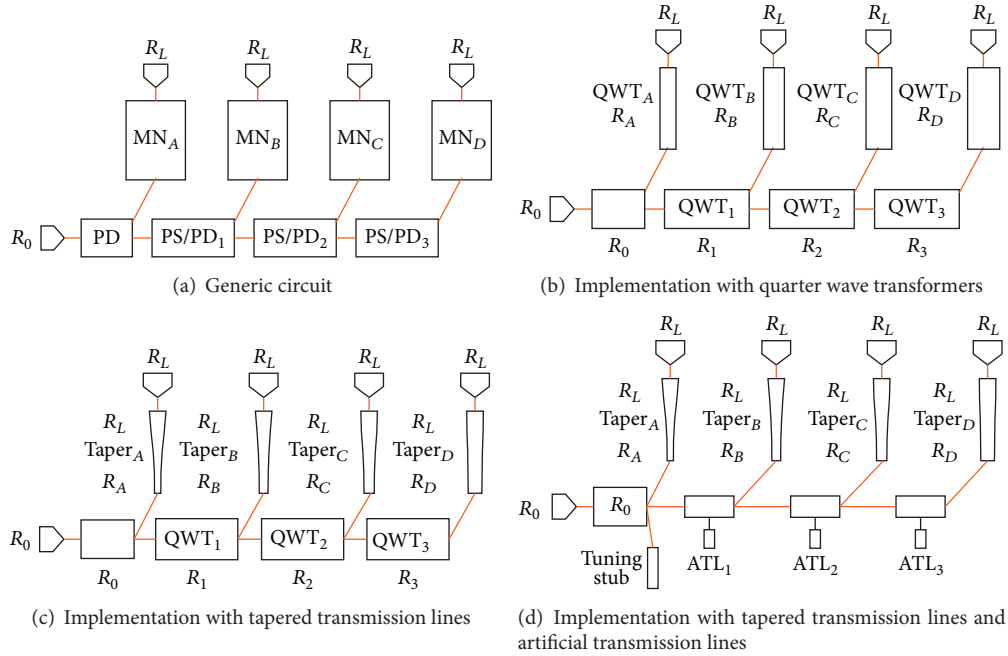

(a) Generic circuit

(b) Implementation with quarter wave transformers

(c) Implementation with tapered transmission lines

(d) Implementation with tapered transmission lines and artificial transmission lines

FIGURE 4: Implementations of the Sequential Phase Network.

which ends with the antenna impedance $Z_L = 100$. The taper length is 30 mm, and the following characteristic resistances are picked: $R_A = 110$, $R_B = 105$, $R_C = 44$, $R_D = 27$, and $R_1 = R_2 = R_3 = 35$.

From the inspection of Figure 5(a) it can be observed that the magnitudes of four transmission parameters are identical only at center frequency, with a wide deviation at the edge of the observed band. The same quantities in Figure 5(b) are less scattered. Fixing the value of 1 dB as the maximum tolerable deviation between the four tracks, the canonic solution exhibits a bandwidth of 1.8 GHz (30% of fractional bandwidth), while the tapered solution is enhanced to 3.2 GHz (53%).

The phase progression of the two solutions, depicted in Figures 6(a) and 6(b), is similar. Despite a higher frequency slope in the second case, which is a consequence of longer (while identical) output lines, the dispersion at the edge of the bandwidth is similar in the two cases.

4. Assembling of the Array

To assemble the array of 16 elements, the subarray of only 2×2 element is designed first, serving as the element of the final arrangement.

4.1. Subarray. Following the analysis of Section 2, a set of four discs tuned to exhibit approximately the response depicted in Figure 3 is designed and sequentially arranged in a square lattice according to the progressive phase principle.

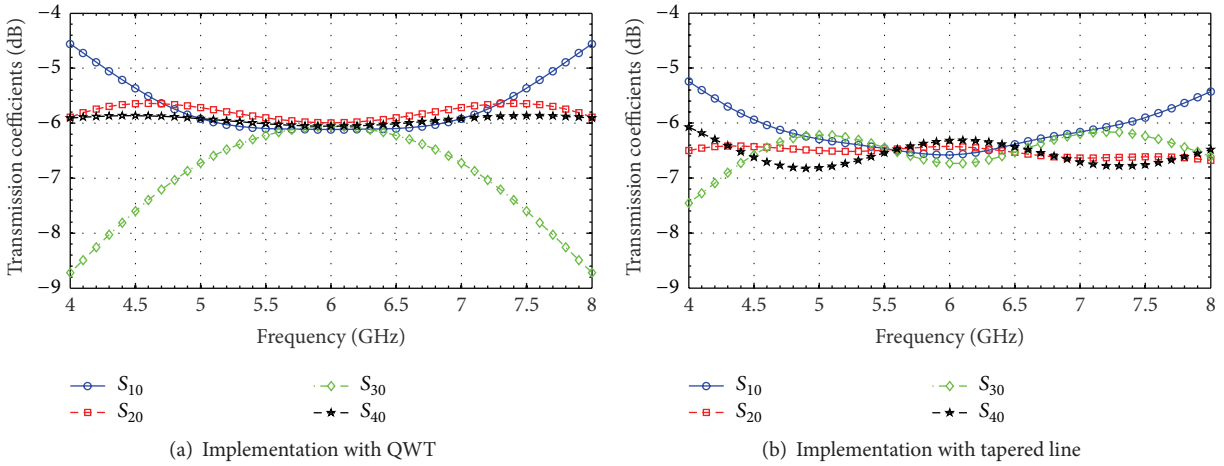

(a) Implementation with QWT (b) Implementation with tapered line

Figure 5: Comparison between canonic network and modified network. Magnitude of the transmission parameters.

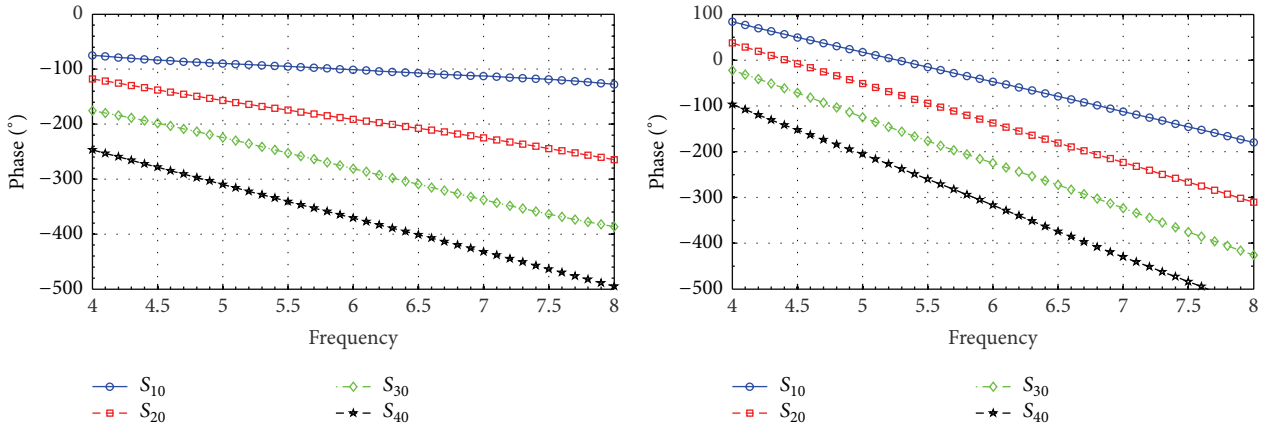

(a) Implementation with QWT (b) Implementation with tapered line

Figure 6: Comparison between canonic network and modified network. Phase of the transmission parameters.

To better accommodate the structure the output tapered lines are curved to better fit between the antenna elements, avoiding waste of space. This geometry is obtained using the following analytical profile (introduced in [21]):

$$x(t) = K^{\pm} \sin\left(\frac{\pi}{2}t\right),$$
$$y(t) = H^{\pm} \cos\left(\frac{\pi}{2}t\right) \sin\left(\frac{\pi}{2}t\right)^{m} \pm W(1-t); \quad (2)$$
$$t \in (0,1).$$

Each equivalent tapered line is implemented adjusting $K^{\pm}$, $H^{\pm}$, and W to provide the adequate matching between the junctions and the antennas.

Furthermore, instead of canonic QWTs, T-section loaded lines are employed for the PSPD (cf. Figure 4(d)). The T-section line consists of the symmetric combination of two TLs loaded with an open-circuit stub. An ATL is physically shorter than canonic QWLs but provides the same nominal 90° phase at center frequency. Despite a low-pass behavior, the use of ATL is not a limiting factor, being its corner frequency compatible with the wideband behavior in Figure 5(b). In addition, high impedance lines, which are used to implement the T-line structure, are an aid to contrast the spurious radiation. As a final tuning a central stub is added after the first junction; see Figure 4(d).

The result of the subarray design stage is depicted in Figure 7, along with the parameters reported in Table 1, obtained after a full-wave optimization with a commercial CAD [27].

Among the various geometric parameters, the element spacing d is very important for the array performance, since it was proven to be the key parameter for the gain and cross-polarization maximization [28]. In [29] it was experimentally proven that the optimal d is $0.7\lambda_0$. Here, for the sake of compactness, a spacing of 20 mm is adopted, about 0.43 λ_0 at 6.5 GHz. While suboptimal, this value permits arranging the subarray in the compact space of $40 \times 40\,\text{mm}^2$, which is compatible with the goal of $80 \times 80\,\text{mm}^2$ for the entire structure.

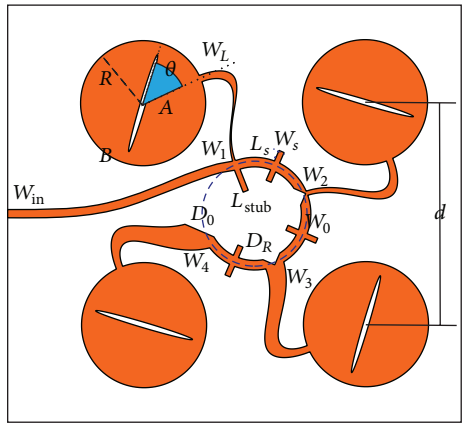

Figure 7: Geometry of the 2 × 2 subarray.

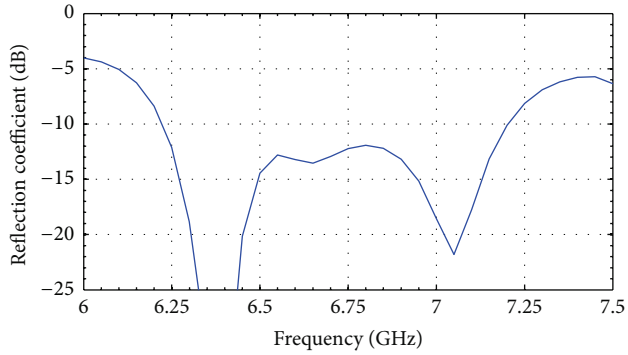

Figure 8: Simulated reflection coefficient of the subarray.

Table 1: List of the geometric parameters of the subarray in Figure 7. The dimensions are in mm, and the angles are in degree.

Param.	R	A	B	θ	W_L	W_{in}	W_0	W_1
Value	7.2	4.6	0.25	44	0.62	0.75	0.88	0.20
Param.	W_2	W_3	W_4	W_S	L_S	w_{stub}	L_{stub}	d
Value	0.42	1.85	2.89	0.40	17.4	0.5	2	20

Figure 8 shows the reflection coefficient of the subarray. A 10 dB return loss of 1 GHz is achieved, recovering for the nonuniform behavior of input impedance observed in Figure 3(a). In Figure 9 the three components of the realized gain are shown, that is, total gain, LH gain, and RH gain. It can be observed that the total gain and the LH gain are coincident at the frequency of 6.7 GHz. The gain is about 9 dB of gain, while the polarization purity exceeds 22 dB.

4.2. Entire Array. The four subarrays described in the previous section are arranged as shown in Figure 10(a). The subarray spacing is 40 mm (d_1), in order to regularly arrange the element in a 20 mm grid. A central SPN based on the same principle applied to the subarray is designed and arranged at the center of the board, to provide the necessary feed to the four sub-SPNs. The available space is adequate to implement the output lines of the central SPN as straight tapered transmission lines (instead of curved lines as for the

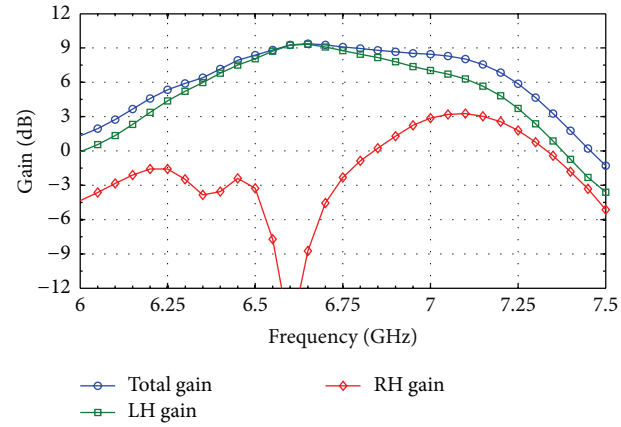

Figure 9: Simulated boresight gain of the subarray.

second-level SPNs). Each line is tapered with a raised-cos profile ending with the same width w_5, which is coincident with the input width w_{in} of the subarrays (cf. Figure 7). The geometry of the structure is depicted in detail in Figure 10(b), and the actual dimensions of the parameters are reported in Table 2. The result structure is very compact, with the antenna elements very close to the transmission lines of both the central and peripheral SPNs.

Starting from the available preliminary design obtained combining the four subarrays, a full-wave optimization has been carried out with a full-wave CAD. The optimization goal is a trade-off between the maximization of the gain and the wider enlargement of the polarization bandwidth. The best design has been fabricated as shown in Figure 11 using standard photo-etching procedures on a high quality substrate (isola FR408: thickness = 1.6 mm, $\epsilon_R = 3.65$, and $\tan\delta = 1E-3$). The entire structure is arranged in a single-layer via-less square PCB of side 80 mm, meaning $3\lambda_0^2$ at 6.5 GHz.

5. Experimental Validation

The measurements of the fabricated prototype were made and compared to the simulations. Figure 12 shows the measured and simulated reflection coefficients of the array. The 10 dB return loss (RL) defines the bandwidth from 4.5 GHz to 7.75 GHz, meaning a very large fractional bandwidth exceeding 53%. A slight frequency shift between simulation and measured is observed. It can be attributed to the design sensibility to the fabrication tolerance. This sensitivity is caused by the coupling of the various structures of the proposed design which are in extreme proximity. For applications tolerant to a slightly worst input matching, the 9 dB RL bandwidth spans from 4.4 GHz to 8.2 GHz, almost the entire *C*-band, which is better than the simulated result.

Figure 13 depicts the frequency behavior of the realized gain in the bore-sight direction. Both the copolar (left-hand) and cross-polar (right-hand) components are depicted. The target "gain/broadband trade-off" is obtained, with a maximum gain of 12.6 dBi at 6.7 GHz and a second maximum of 12 dBi at 6.20 GHz. The gain deviation is inside the range

Table 2: List of the geometric parameters of the central network in Figure 10. The dimensions are in mm.

Parameter	W_{input}	W_0	W_1	W_2	W_3	W_4	W_5	w_S	L_S	d_0	d_1	D_1	L_{sub}
Value	1.80	0.90	0.25	0.40	1.80	2.80	0.75	0.40	17.0	20	40	4.70	80

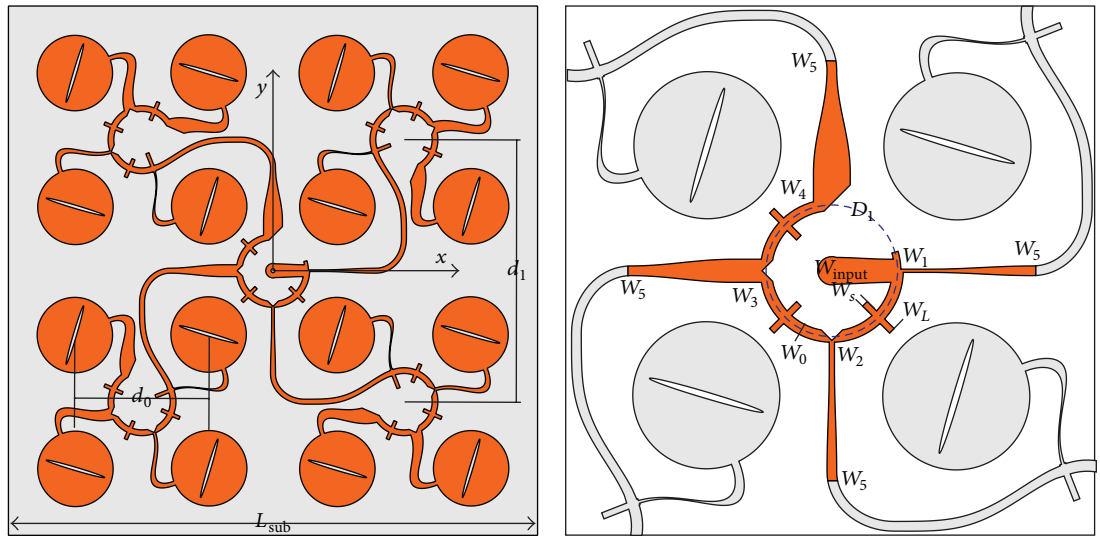

(a) Final assembling design (b) Detail of the central SPN

Figure 10: Detail of the central area.

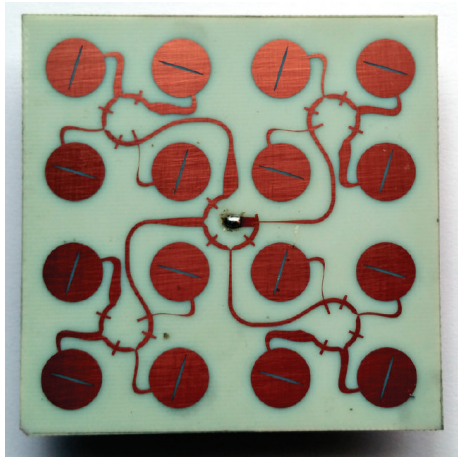

Figure 11: Photograph of the proposed prototype.

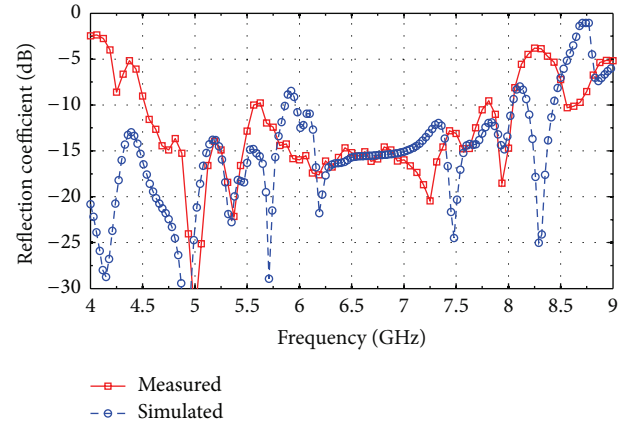

Figure 12: Simulated and measured reflection coefficients.

of 3 dB in the frequency bandwidth from 6.0 GHz to 7.0 GHz, about 1 GHz. Comparing simulated and experimental results, it can be observed that the simulation presents a narrower region characterized by higher gain, while the experimental behavior exhibits a wider bandwidth affected by a deviation. Nevertheless, considering the relatively limited entity of the ripple, the experimental result can be considered satisfactory.

The measured axial ratio, depicted in Figure 14, is affected by the tolerance fabrication. Fixing the tolerated deviation of nominal axial ratio at 4 dB, the polarization bandwidth spans from 5.18 GHz to 7.1 GHz, almost 2.0 GHz of left-hand polarization which represents a fractional bandwidth of about 30%. Following the strict 3 dB definition, the bandwidth splits in two regions (from 5.25 GHz to 6.2 GHz and from 6.3 GHz to 7.05 GHz), because of an axial ratio relative maximum around 6.25 GHz. Considering the extreme level of coupling the wideband behavior demonstrates the validity of the proposed design. In Figure 15, the measured pattern of the prototype is depicted for various central frequencies among the C-band. For each case, the co- and cross-, x-, and y-cuts are given. It can be observed that the pattern shape is maintained over the

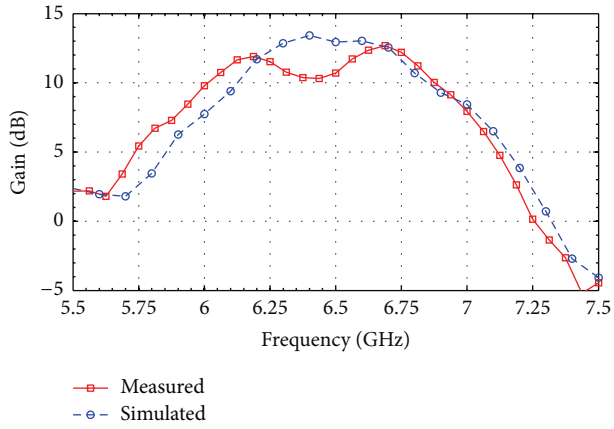

Figure 13: Simulated and measured bore-sight gains.

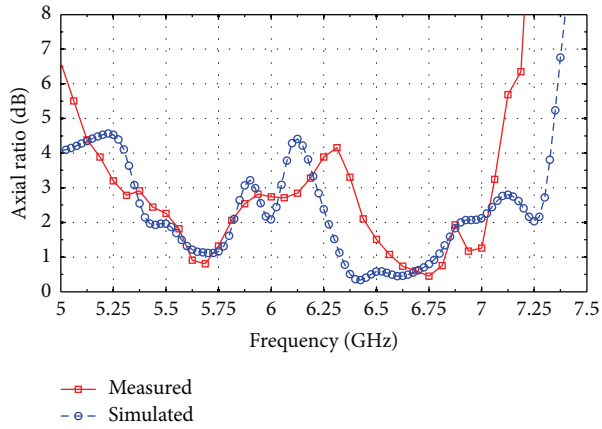

Figure 14: Simulated and measured bore-sight axial ratio.

entire band, despite the gain reduction depicted in Figure 13. This feature is obtained thanks to the two levels of SPN which are tolerant to the element overtuning.

6. Conclusions

A compact wideband circularly polarized antenna array for application in the *C*-band was designed, simulated, and fabricated. The array is based on the recursive application of the sequential phase arrangement on a compact disc patch element capable of broad while imperfect circular polarization.

The fabricated array occupies a square of 80 mm × 80 mm and hence a surface of $3\lambda_0^2$ at the mean frequency of 6.5 GHz. A peak gain of 12.6 dB is achieved at the frequency of 6.7 GHz and a second peak of 12 dB at 6.2 GHz. Furthermore, the LH gain is above 8 dB from 5.9 GHz to 7.0 GHz, meaning more than 1.0 GHz. Moderate polarization purity is observed over a wide band of frequency. Excluding a "notch" region around 6.25 GHz, the 3 dB AR bandwidth spans from 5.25 GHz to 7.0 GHz, meaning 28%. A more conservative bandwidth tolerant to 4 dB of AR spans from 5.18 GHz to 7.1 GHz, meaning 31%.

Table 3: A comparison of the proposed array with other similar arrays.

2 × 2 array	[25]	[26]	The present paper
10 dB RL BW (GHz)	4.82–5.12	4.40–5.45	4.50–8.00
4 dB AR BW (GHz)	4.78–5.22	4.40–5.50	5.20–7.05
Max gain (dB)	10.5	11.5	12.6
3 dB gain BW (GHz)	4.86–5.12	4.80–5.50	6.00–6.90
Global BW (%)	5.2%	13.5%	14.0%
Size (cm^2)	100 cm^2	81 cm^2	64 cm^2
Size (λ_0^2)	2.7 λ_0^2	3.2 λ_0^2	3.0 λ_0^2

The compact dimension of the proposed design affects the gain and polarization performance, for both suboptimal arrangement and strong mutual coupling. However, if compared to similar single-layer array with similar occupied area, the proposed array presents a more convenient performance/dimension trade-off. In particular, a better max gain and a wider global bandwidth are observed despite a smaller normalized area (cf. Table 3).

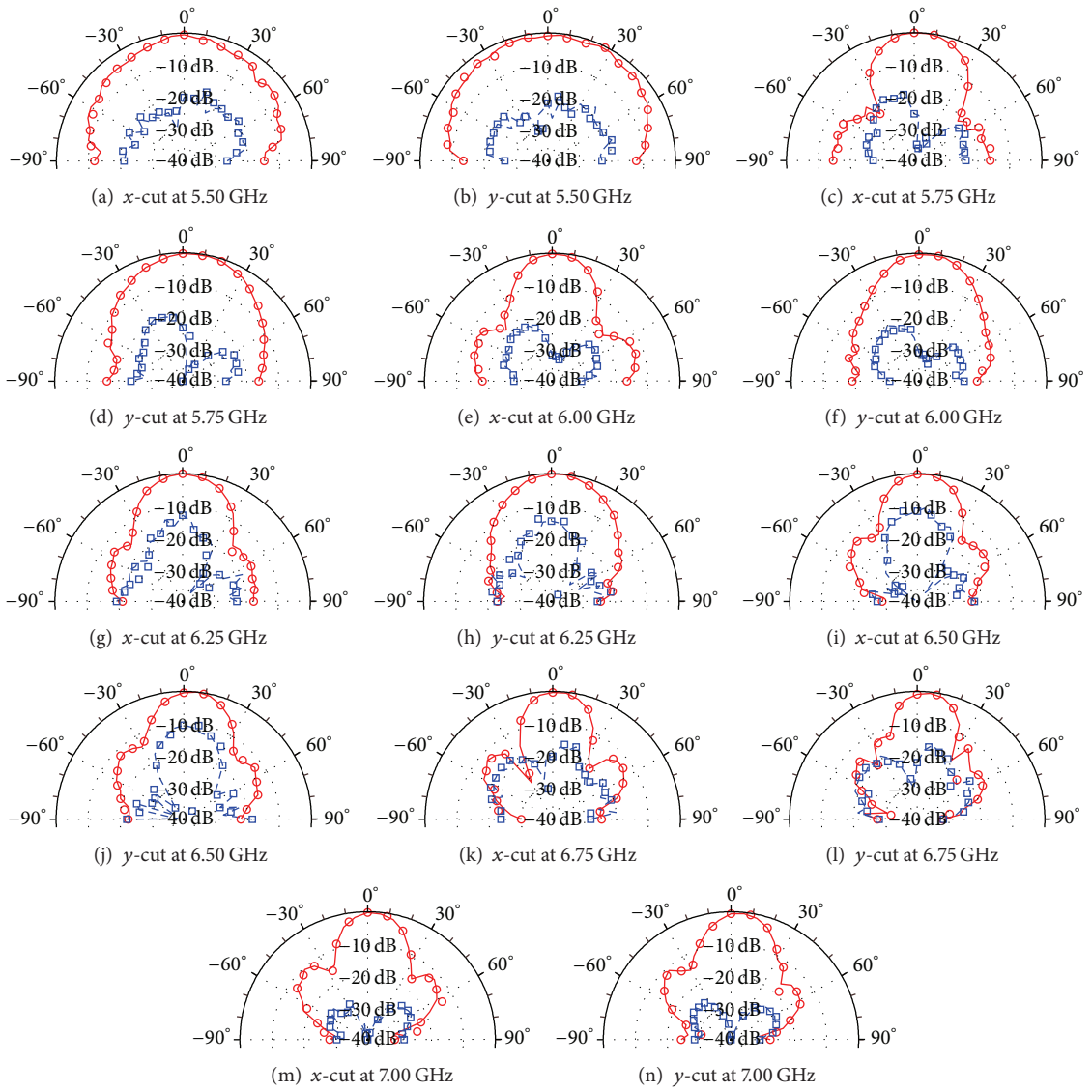

FIGURE 15: Principal cuts of the proposed array, according to the reference in Figure 10(a). Solid line with dots: copolar (LH). Dashed line with squares: cross-polar (RH).

Conflict of Interests

The author declares that there is no conflict of interests regarding the publication of this paper.

References

[1] P. J. Gibson, "The vivaldi aerial," in *Proceedings of the 9th IEEE European Microwave Conference*, pp. 101–105, IEEE, Brighton, UK, September 1979.

[2] M. J. Ammann and Z. N. Chen, "Wideband monopole antennas for multiband wireless systems," *IEEE Antennas and Propagation Magazine*, vol. 45, no. 2, pp. 146–150, 2003.

[3] J.-Y. Deng, Y.-Z. Yin, Y.-H. Huang, J. Ma, and Q.-Z. Liu, "Compact circularly polarized microstrip antenna with wide beamwidth for compass satellite service," *Progress In Electromagnetics Research Letters*, vol. 11, pp. 113–118, 2009.

[4] F. Ferrero, C. Luxey, G. Jacquemod, and R. Staraj, "Dual-band circularly polarized microstrip antenna for satellite applications," *IEEE Antennas and Wireless Propagation Letters*, vol. 4, no. 1, pp. 13–15, 2005.

[5] L. Bencini, S. Maddio, G. Collodi, D. Di Palma, G. Manes, and A. Manes, "Development of wireless sensor networks for agricultural monitoring," in *Smart Sensing Technology for Agriculture and Environmental Monitoring*, pp. 157–186, Springer, 2012.

[6] S. Maddio, A. Cidronali, and G. Manes, "Smart antennas for direction-of-arrival indoor positioning applications," in *Handbook of Position Location: Theory, Practice, and Advances*, pp. 319–355, Wiley, 2011.

[7] A. Cidronali, S. Maddio, G. Giorgetti, I. Magrini, S. K. S. Gupta, and G. Manes, "A 2.45 GHz smart antenna for location-aware single-anchor indoor applications," in *Proceedings of the IEEE MTT-S International Microwave Symposium (IMS '09)*, pp. 1553–1556, Boston, Mass, USA, June 2009.

[8] Electromagnetic Compatibility and Radio Spectrum Matters (ERM) and Road Transport and Traffic Telematics (RTTT), "EN300674-1 V1.2.I, Dedicated Short Range Communication (DSRC) transmission equipment (500 kbitls/250 kbitls) operating in the 5,8 GHz Industrial," Scientific and Medical (ISM) Band, ETSI.

[9] R. Garg, *Microstrip Antenna Design Handbook*, Artech House, 2001.

[10] A. Chen, Y. Zhang, Z. Chen, and S. Cao, "A Ka-band high-gain circularly polarized microstrip antenna array," *IEEE Antennas and Wireless Propagation Letters*, vol. 9, pp. 1115–1118, 2010.

[11] J.-W. Baik, T.-H. Lee, S. Pyo, S.-M. Han, J. Jeong, and Y.-S. Kim, "Broadband circularly polarized crossed dipole with parasitic loop resonators and its arrays," *IEEE Transactions on Antennas and Propagation*, vol. 59, no. 1, pp. 80–88, 2011.

[12] C. Liu, A. Yan, C. Yu, and T. Xu, "Improvement on a 2 × 2 Elements high-gain circularly polarized antenna array," *International Journal of Antennas and Propagation*, vol. 2015, Article ID 252717, 8 pages, 2015.

[13] V. Rafii, J. Nourinia, C. Ghobadi, J. Pourahmadazar, and B. S. Virdee, "Broadband circularly polarized slot antenna array using sequentially rotated technique for C-Band applications," *IEEE Antennas and Wireless Propagation Letters*, vol. 12, pp. 128–131, 2013.

[14] D.-Y. Kim, J. W. Lee, T. K. Lee, and C. S. Cho, "Design of SIW cavity-backed circular-polarized antennas using two different feeding transitions," *IEEE Transactions on Antennas and Propagation*, vol. 59, no. 4, pp. 1398–1403, 2011.

[15] D. Kim, J. W. Lee, C. S. Cho, and T. K. Lee, "X-band circular ring-slot antenna embedded in single-layered SIW for circular polarisation," *Electronics Letters*, vol. 45, no. 13, pp. 668–669, 2009.

[16] A. Chen, Y. Zhang, Z. Chen, and C. Yang, "Development of a K_a band wideband circularly polarized 64-element microstrip antenna array with double application of the sequential rotation feeding technique," *IEEE Antennas and Wireless Propagation Letters*, vol. 10, pp. 1270–1273, 2011.

[17] Z. Yanjun, C. Aixin, C. Shunfeng, and S. Donglin, "Design of a circularly polarized 8 × 8 patch antenna array using a new series-parallel feed," in *Proceedings of the 3rd IEEE International Symposium on Microwave, Antenna, Propagation and EMC Technologies for Wireless Communications (MAPE '09)*, pp. 411–414, Beijing, China, October 2009.

[18] S. Maddio, A. Cidronali, and G. Manes, "A new design method for single-feed circular polarization microstrip antenna with an arbitrary impedance matching condition," *IEEE Transactions on Antennas and Propagation*, vol. 59, no. 2, pp. 379–389, 2011.

[19] S. Maddio, A. Cidronali, and G. Manes, "An azimuth of arrival detector based on a compact complementary antenna system," in *Proceedings of the IEEE European Wireless Technology Conference (EuWIT '10)*, Paris, France, September 2010.

[20] E. Levine, G. Malamud, S. Shtrikman, and D. Treves, "Study of microstrip array antennas with the feed network," *IEEE Transactions on Antennas and Propagation*, vol. 37, no. 4, pp. 426–434, 1989.

[21] S. Maddio, "A compact wideband circularly polarized antenna array for *C*-band applications," *IEEE Antennas and Wireless Propagation Letters*, vol. 14, pp. 1081–1084, 2015.

[22] T. Zhang, W. Hong, and K. Wu, "Analysis and optimum design of sequential-rotation array for gain bandwidth enhancement," *IEEE Transactions on Antennas and Propagation*, vol. 63, no. 1, pp. 142–150, 2015.

[23] P. Xu, Z.-H. Yan, T.-L. Zhang, and X.-Q. Yang, "Broadband circularly polarized slot antenna array using a compact sequential-phase feeding network," *Progress in Electromagnetics Research C*, vol. 47, pp. 173–179, 2014.

[24] S. Maddio, "A circularly polarized antenna array with a convenient bandwidth/size ratio based on non-identical disc elements," *Progress In Electromagnetics Research Letters*, vol. 57, no. 1, pp. 47–54, 2015.

[25] Y. Li, Z. Zhang, and Z. Feng, "A sequential-phase feed using a circularly polarized shorted loop structure," *IEEE Transactions on Antennas and Propagation*, vol. 61, no. 3, pp. 1443–1447, 2013.

[26] W. Yang, J. Zhou, Z. Yu, and L. Li, "Bandwidth and gain enhanced circularly polarized antenna array using sequential phase feed," *IEEE Antennas and Wireless Propagation Letters*, vol. 13, pp. 1215–1218, 2014.

[27] Ansoft, 2014, http://www.ansys.com/.

[28] S.-K. Lin and Y.-C. Lin, "A compact sequential-phase feed using uniform transmission lines for circularly polarized sequential-rotation arrays," *IEEE Transactions on Antennas and Propagation*, vol. 59, no. 7, pp. 2721–2724, 2011.

[29] A. R. Weily and Y. J. Guo, "Circularly polarized ellipse-loaded circular slot array for millimeter-wave WPAN applications," *IEEE Transactions on Antennas and Propagation*, vol. 57, no. 10, pp. 2862–2870, 2009.